Charge density waves and phonon-electron coupling in $ZrTe_3$

Yuwen Hu,[1] Feipeng Zheng,[1] Xiao Ren,[1] Ji Feng,[1,2,*] and Yuan Li[1,2,†]
[1]*International Center for Quantum Materials, School of Physics, Peking University, Beijing 100871, China*
[2]*Collaborative Innovation Center of Quantum Matter, Beijing 100871, China*
(Received 20 February 2015; published 3 April 2015)

Charge-density-wave (CDW) order has long been interpreted as arising from a Fermi-surface instability in an initiating metallic phase. While phonon-electron coupling has been recently suggested to influence the formation of CDW order in quasi-two-dimensional (quasi-2D) systems, the presumed dominant importance of Fermi-surface nesting remains largely unquestioned in quasi-1D systems. A key step toward this quest requires a close-knit synthesis of spectroscopic evidence and microscopic knowledge about the electronic structure and the lattice dynamics in a prototypical system. Here we take this approach to show that phonon-electron coupling is also important for the CDW formation in a model quasi-1D system $ZrTe_3$, with joint experimental and computational investigation. It is revealed that singularly strong coupling between particular lattice-distortion patterns and conduction electrons gives rise to anomalously broad Raman phonon peaks, which exhibit a distinct anisotropy in both the measured and the computed linewidths. The dependence of the coupling strength on electron momentum further dictates the opening of (partial) electronic gaps in the CDW phase. Since lattice distortion and electronic gaps are defining signatures of CDW order, our results demonstrate that while Fermi-surface nesting determines the CDW periodicity in this quasi-1D system, the conventional wisdom needs to be substantially supplemented by phonon-electron coupling for a quantitative understanding of the CDW order.

DOI: 10.1103/PhysRevB.91.144502 PACS number(s): 63.20.kd, 71.45.Lr, 63.20.dk, 78.30.−j

I. INTRODUCTION

The mechanism for the formation of charge-density-wave (CDW) order in metals is a long-standing problem in condensed matter physics. The recent discovery of ubiquitous charge-ordering phenomena in cuprate high-temperature superconductors [1–6] has aroused new interest in this problem, since a thorough and generic understanding of the formation of CDW order, even in simple metals, may shed light on several important issues relevant to the enigma of high-temperature superconductivity. In particular, the so-called pseudogap phenomena in underdoped cuprates [7], which precede superconductivity upon cooling, resemble the opening of partial electronic energy gaps on certain parts of Fermi surfaces in CDW metals [8–10]. While long-range static CDW order appears to compete with superconductivity [2,5,11], short-range CDW correlations are present over a substantial range of carrier concentrations [2,12] that support the appearance of superconductivity, which points to the intriguing possibility that the two phases might share a common microscopic origin. It is, therefore, important to identify the necessary and sufficient conditions for driving a CDW transition, and to understand how a material's electronic structure can be affected upon approaching such transitions.

CDW order is most commonly found in metals with highly anisotropic, or "low-dimensional," electronic structure. Typical examples include quasi-one-dimensional (quasi-1D) $K_2Pt(CN)_4$ [13], blue bronzes [14], and transition-metal trichalcogenides [15,16], as well as quasi-2D transition-metal dichalcogenides [17] and rare-earth tritellurides [18]. In the classical explanation first introduced by Peierls [19], CDW transitions are understood as arising from the presence of a pair of nearly parallel Fermi surfaces, known as Fermi-surface nesting (FSN), which causes the dielectric response of conduction electrons to diverge at the nesting wave vector $\mathbf{q}_n$. Even though a periodic modulation of the electron density can be stabilized only by coupling to the crystal lattice [20], it is $\mathbf{q}_n$ that determines the periodicity of the modulation; i.e., in the Peierls picture CDW order is primarily electronically driven. In most quasi-1D and some quasi-2D systems, a good agreement between the CDW wave vector $\mathbf{q}_{cdw}$ and $\mathbf{q}_n$ has indeed been found [10,21,22], in support of the Peierls picture.

However, similar agreement between $\mathbf{q}_{cdw}$ and $\mathbf{q}_n$ is not supported by highly accurate measurements [8,23] and calculations [24] on the prototypical quasi-2D CDW compound $NbSe_2$. First-principles calculations have cast further doubt on the generic validity of using FSN as the sole criterion for potential Peierls instability [25]: on the one hand, FSN leads to a pronounced enhancement in the imaginary part of the electronic susceptibility near $\mathbf{q}_n$, but the formation of CDW order requires a large real part of the susceptibility which does not solely depend on FSN; on the other hand, the susceptibility enhancement due to FSN is usually weak in real materials, and it is excessively fragile against imperfect nesting, impurity scattering, and thermal-broadening effects. It is important to realize that the most predictive signature of potential CDW instability is the presence of soft phonon modes in the initiating phase [26]. In this line of thinking, it is only natural to recognize the essential role of phonon-electron coupling in the formation of CDW order, as suggested by several authors [25,27]. This idea has been explicitly tested in quasi-2D materials both theoretically [24,28–30] and experimentally [30–32], and has proved quite successful in explaining the $\mathbf{q}_{cdw}$ that deviates from $\mathbf{q}_n$.

In quasi-1D materials, the importance of phonon-electron coupling relative to that of FSN has remained largely untested,

*jfeng11@pku.edu.cn
†yuan.li@pku.edu.cn

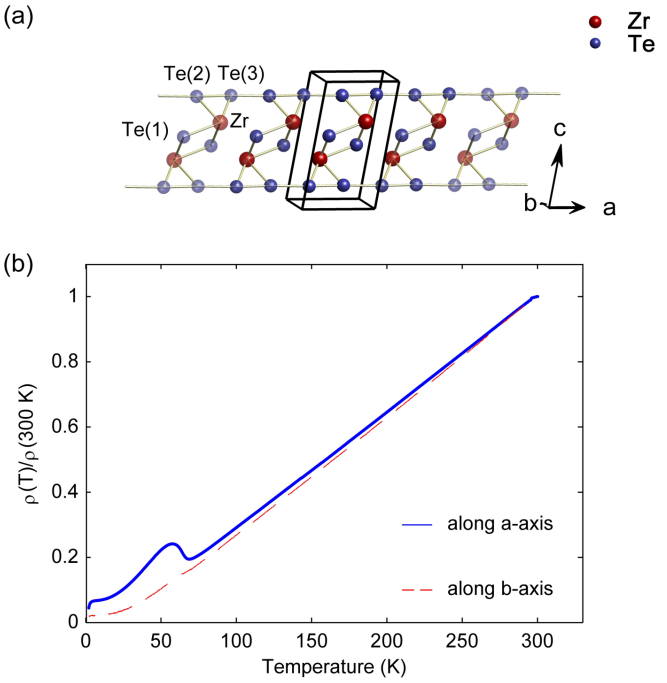

FIG. 1. (Color online) (a) A schematic view of the crystal structure of $ZrTe_3$. (b) Temperature dependence of resistivity measured with currents flowing along the crystallographic a and b axes, normalized at 300 K.

as the good agreement between $\mathbf{q}_n$ and $\mathbf{q}_{cdw}$ in 1D cases might appear to render such tests unnecessary. One may note, however, that even in a simple quasi-1D system, the Peierls picture lacks such predicting power as to identify lattice distortions that are associated with the CDW order. Moreover, CDW energy gaps are often found on only certain parts of the Fermi surface [10,21], even when the remaining parts are equally-well nested, which cannot be explained by the Peierls picture. These inadequacies have motivated us to perform a detailed study of phonon-electron coupling in the prototypical quasi-1D CDW compound $ZrTe_3$. $ZrTe_3$ possesses a monoclinic structure with $a = 5.89$ Å, $b = 3.93$ Å, $c = 10.09$ Å, $\alpha = \gamma = 90°$, and $\beta = 82.2°$ [Fig. 1(a)]. CDW order is stabilized below $T_{cdw} = 63$ K with $\mathbf{q}_{cdw} = (0.07a^*, 0, 0.33c^*)$ [33], which is in good agreement with $\mathbf{q}_n$ that connects quasi-1D Fermi surfaces arising from the $5p$ orbitals of Te(2)/Te(3) atoms that form a chainlike structure along the a axis.

Here we combine variable-temperature Raman scattering measurements and first-principles calculations [34] to investigate the influence of phonon-electron coupling on the CDW formation in $ZrTe_3$. Despite the material's simple crystal structure, its lattice dynamics have not been studied using first-principles calculations. A back-to-back comparison of our experimental and computational results yields excellent agreement, which allows us to reliably determine both phonon eigenvectors and phonon-electron coupling matrix elements. We find that phonon-electron coupling indeed plays a substantial role, and is necessary to consider in conjunction with FSN, in order to reach a quantitative understanding of the CDW formation in this quasi-1D case.

II. METHODS

A. Experimental methods

Single crystals of $ZrTe_3$ were grown by a chemical vapor transport method using iodine as transport gas. The high and low temperatures used in the growth process are 735 and 660 °C, respectively, which correspond to the low-temperature growth method in Ref. [35]. The crystals were characterized by x-ray powder diffraction and resistivity measurements, which confirmed that our crystals were of single phase and high quality. The x-ray diffraction measurements were performed on a Rigaku MiniFlex diffractometer at room temperature. The resistivity measurement was performed with a standard four-probe method using a Quantum Design PPMS.

Our Raman scattering measurements were performed in a confocal back-scattering geometry on freshly cleaved crystal surfaces using the $\lambda = 514$ nm line of an Ar laser for excitation. In order to obtain spectra with light polarizations along various crystallographic axes, crystals were cleaved both parallel and perpendicular to the ab plane. The Raman spectra were analyzed using a Horiba Jobin Yvon LabRAM HR Evolution spectrometer, equipped with 1800 gr/mm gratings, a liquid-nitrogen-cooled CCD detector, and BragGrate notch filters that allow for measurements down to low wave numbers. The temperature of the sample was controlled by a liquid-helium flow cryostat, with the sample kept under better than 5×10^{-7} Torr vacuum at all times. Consistent Raman spectra have been obtained on several different samples, as well as with different excitation-photon wavelengths (633 and 785 nm).

B. Density-functional theory calculations

Density-functional theory calculations were performed using Quantum Espresso [34], within the generalized-gradient approximation parametrized by Perdew, Burke, and Ernzerhof [36,37], to investigate the electronic structure, BZ-center phonons, and phonon-electron coupling in $ZrTe_3$. Norm-conserving pseudopotentials, generated by the method of Goedecker, Hartwigsen, Hutter, and Teter [38], were used to model the interactions between valence electrons and ionic cores of both Zr and Te atoms. The Kohn-Sham valence states were expanded in the plane wave basis set with a kinetic energy truncation at 150 Ry. The Raman-active phonons were calculated at the BZ center using a linear-response approach. The equilibrium crystal structure was determined by a conjugated-gradient relaxation, until the Hellmann-Feynman force on each atom was less than 0.8×10^{-4} eV/Å and zero-stress tensor was obtained. A $12 \times 18 \times 8$ **k** grid centered at the Γ point was chosen, in combination with a Gaussian-type broadening of 0.0055 Ry.

The phonon linewidth (defined as full width at half maximum, FWHM, in the Raman spectra), $\gamma_{\mathbf{q}\nu}$, is twice the imaginary part of the phonon self-energy arising from phonon-electron interactions:

$$\gamma_{\mathbf{q}\nu} = \frac{4\pi}{N_k} \sum_{\mathbf{k}mn} \left| g^{\nu}_{\mathbf{k}n,\mathbf{k}+\mathbf{q}m} \right|^2 (f_{\mathbf{k}n} - f_{\mathbf{k}+\mathbf{q}m}) \delta(\epsilon_{\mathbf{k}+\mathbf{q}m} - \epsilon_{\mathbf{k}n} - \omega_{\mathbf{q}\nu}), \quad (1)$$

where the summation is over a set of **k** points forming a regular grid in the BZ, each with a pair of Kohn-Sham

electronic states m and n whose crystal momenta differ by that of the phonon mode $\mathbf{q}$. The phonon-electron coupling matrix elements, $g^{\nu}_{\mathbf{k}n,\mathbf{k}+\mathbf{q}m} = \langle \mathbf{k}n|\delta V/\delta u_{\mathbf{q}\nu}|\mathbf{k}+\mathbf{q}m\rangle/\sqrt{2\omega_{\mathbf{q}\nu}}$, are obtained from Quantum Espresso [34], where $u_{\mathbf{q}\nu}$ is the atomic displacements of mode ν at a wave vector $\mathbf{q}$. The Fermi-Dirac distribution, $f_{\mathbf{k}n}$, gives the occupation of the Kohn-Sham state with $\epsilon_{\mathbf{k}n}$. The summation in Eq. (1) can be quite singular, and we used the cubic-spline to interpolate the electronic spectra and the squared phonon-electron coupling matrix elements from a coarse $\mathbf{k}$ grid of $44 \times 68 \times 24$ to $660 \times 1020 \times 360$, where $\epsilon_{\mathbf{k}n}$ were calculated. Finally, the weighted average of $\gamma_{\mathbf{q}\nu}$ from a small region of $\mathbf{q}$ near the BZ center was used to estimate the actual phonon linewidth measured in Raman scattering experiments.

C. Mode averaging of phonon linewidths

To reproduce the experimentally observed phonon linewidths, it is critical to realize that Raman scattering probes phonons in the small- but nonzero-$\mathbf{q}$ regime. In this regime, while the phonon-electron coupling matrix elements are well approximated by the $q = 0$ values, the summation of γ in Eq. (1) differs dramatically from the $q = 0$ limit owing to intraband transitions. To account for this effect, we have weight-averaged γ evaluated at a set of small $\mathbf{q}$ near $q = 0$, with a maximum of $|q| = 6 \times 10^{-3} a_0^{-1}$ ($a_0 = 0.5292$ Å is the Bohr radius) which corresponds to the back-scattering of 514 nm photons. An index of refraction of 4.6 is used for calculating the momentum carried by 514 nm photons propagating inside $ZrTe_3$ [39], and it is assumed that the matrix elements in this small region of $\mathbf{q}$ are the same as those at $q = 0$.

We now describe how the Raman peak width is estimated with a weighted average of the computed phonon linewidths. In a Raman process, the incident photon has a small but finite momentum $\mathbf{q}_i$, and the scattered photon is emitted with a momentum $\mathbf{q}_s$. The phonon involved then has a crystal momentum $\mathbf{q} = \mathbf{q}_s - \mathbf{q}_i$. Because of the phonon-electron coupling, the phonon has a finite lifetime giving rise to a linewidth (FWHM) that is twice the imaginary part of the self-energy, which is calculated using the linear-response theory as described above. This leads to a statistical spread of the photon energy being emitted. Therefore, the Raman scattered photon in each momentum channel has an intensity profile

$$I_{\mathbf{q}_s}(\omega) = g_{\mathbf{q}_s}(\omega)\delta r(\mathbf{q}_s), \tag{2}$$

where $\delta r(\mathbf{q}_s)$ is the emitting rate of photons with momentum $\mathbf{q}_s$, and $g_{\mathbf{q}_s}(\omega)$ is a normalized distribution with standard deviation that approximately equals the phonon lifetime, $\sigma(\mathbf{q}_s) \approx \gamma(\mathbf{q})$, where $\mathbf{q}$ and $\mathbf{q}_s$ are interrelated by the momentum conservation. The measured intensity is a simple superposition of photons coming in individual momentum channels,

$$I(\omega) = \sum_{\mathbf{q}_s} I_{\mathbf{q}_s}(\omega), \tag{3}$$

where the summation is over all $|\mathbf{q}_s| = |\mathbf{q}_i|$, or equivalently, over a sphere in phonon momentum $\mathbf{q}$ space centered around $-\mathbf{q}_i$ with radius $|\mathbf{q}_i|$. This summation is based on the assumption that scattered photons propagating in all directions are collected with equal efficiency, which is slightly different from the actual back-scattering experimental configuration in which photons with $\mathbf{q}_s = -\mathbf{q}_i$ are more likely to be collected by the objective lens of our spectrometer. It is nevertheless a reasonable approximation because the scattered photons are subject to elastic diffuse scattering which randomizes their propagating directions.

Take a photon collected by the spectrometer in the experiment; it has a probability of coming from the momentum channel $\mathbf{q}_s$

$$p(\mathbf{q}_s) = \frac{\delta r(\mathbf{q}_s)}{\sum_{\mathbf{q}'_s} \delta r(\mathbf{q}'_s)}. \tag{4}$$

Let ω be the energy of this photon; its contribution to the sum of error squares is given by $(\omega - \bar{\omega})^2$, with an associated weight $p(\mathbf{q}_s)$. Thus, assuming identical $\bar{\omega}$ for all $\mathbf{q}_s$ in the small-q limit, it follows that

$$\sigma[I(\omega)] = \sqrt{\frac{\sum_{\mathbf{q}_s} \delta r(\mathbf{q}_s)\sigma^2(\mathbf{q}_s)}{\sum_{\mathbf{q}_s} \delta r(\mathbf{q}_s)}}. \tag{5}$$

We have stipulated that

$$\mathrm{var}[I_s(\omega)] \equiv \sigma^2(\mathbf{q}_s) \equiv N_s^{-1} \sum_{n_s=1}^{N_s} (\omega_{n_s} - \bar{\omega})^2 \approx \gamma^2(\mathbf{q}), \tag{6}$$

where $\mathbf{q} = \mathbf{q}_s - \mathbf{q}_i$, and n_s denotes energy transfer of all possible scattering processes with $\mathbf{q}_s$.

As the photon is Raman scattered by a phonon, the process is inherently mediated by the electrons. Thus, as a first approximation, we assume that the rate of emission from a momentum channel, $\delta r(\mathbf{q}_s)$, is proportional to the strength of the phonon-electron coupling, as measured by $\gamma(\mathbf{q})$. We then arrive at a weighted-average estimate of the standard deviation of the measured Raman peak

$$\sigma[I(\omega)] = \sqrt{\frac{\sum_{\mathbf{q}_s} \gamma^3(\mathbf{q})}{\sum_{\mathbf{q}_s} \gamma(\mathbf{q})}}. \tag{7}$$

Considering that the measured Raman peak is better fitted with a Lorentzian than Gaussian distribution, a remark on this estimate is in order. A Lorentzian does not have a well-defined standard deviation. But since neither the experimental peak nor the superposed intensity in the above construction constitutes a true Lorentzian, the standard deviation computed this way would be a reasonable estimate of the FWHM.

III. RESULTS AND DISCUSSION

A. Sample characterization

We measured the resistivity of single crystals in a temperature range between 2 K and 300 K [Fig. 1(b)]. A clear resistivity anomaly is observed around $T_{\mathrm{CDW}} = 63$ K when the electric current flows along the crystallographic a axis. In contrast, a similar resistivity anomaly is very weak or absent in the b axis. Filamentary superconductivity is observed below $T \approx 3$ K. These results are consistent with previous reports [16,40]. The small residual resistance at low temperatures demonstrates the high quality of our samples.

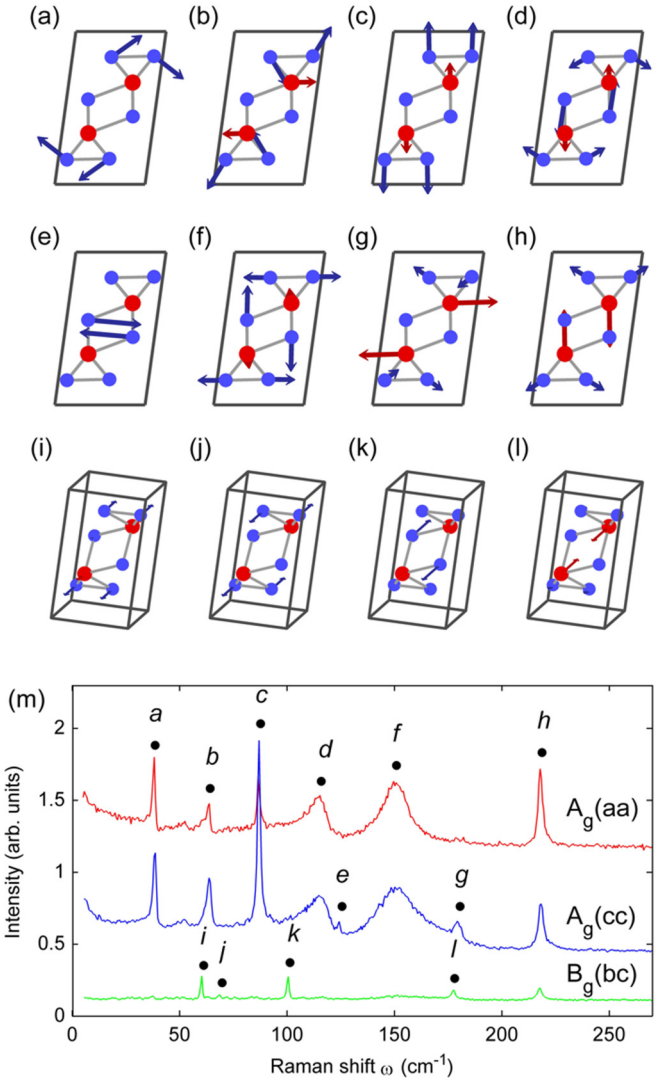

FIG. 2. (Color online) Calculated vibrational patterns of eight A_g [(a)–(h)] and four B_g [(i)–(l)] phonon modes, from low to high energy. (m) Polarized Raman spectra obtained at 70 K, offset for clarity. Letters indicate the corresponding calculated vibrational patterns.

B. Identification of Raman-active phonons

The crystal structure of $ZrTe_3$ belongs to the space group $P12_1/m1$, with all atoms occupying Wyckoff $2e$ positions. Group theory analysis shows that there are a total of twelve Raman-active modes in $ZrTe_3$, including eight A_g modes and four B_g modes, which involve atomic movements in the ac plane and along the b axis, respectively. Only linear photon polarizations are employed in our Raman scattering measurements, and the combination of incident- and scattered-photon polarizations is denoted by two letters that indicate the polarization directions with respect to the crystallographic axes. A_g modes can be observed in aa, bb, and cc polarizations, whereas B_g modes can be observed in ab and bc polarizations.

Figure 2(m) displays Raman spectra obtained at $T = 70$ K $> T_{cdw}$ in the aa, cc, and bc polarization geometries. The spectrum obtained in the aa geometry is consistent with previous reports [41,42] and reveals a total of six phonon peaks, but it fails to detect two remaining A_g modes, presumably due to unfavorable Raman-scattering matrix elements. These two modes become clearly visible in the cc spectrum. The spectrum taken in bc geometry reveals all four B_g modes, which are found at different frequencies than those of the peaks in the aa and cc spectra. Cross-leakage signals are ignored in our identification of phonons.

TABLE I. Experimental and calculated phonon frequencies, ω, and linewidths, γ, at 150 K, all given in units of cm^{-1}.

A_g Phonon	a	b	c	d	e[a]	f	g[a]	h
ω_{exp}	38	63	86	116	123	147	177	217
ω_{cal}	38	56	70	103	107	142	169	201
γ_{exp}, $\mathbf{q}\|\|\mathbf{a}^*$	1.6	2.5	1.8	15		30		3.3
γ_{exp}, $\mathbf{q}\|\|\mathbf{c}^*$	1.3	2.4	2.4	16		20.5		3.5
γ_{cal}, $\mathbf{q}\|\|\mathbf{a}^*$	1.7	1.0	0.9	11.8	0.4	20.5	0.3	4.1
γ_{cal}, $\mathbf{q}\|\|\mathbf{c}^*$	1.1	0.9	0.7	10.8	0.4	14.5	0.2	4.8
B_g Phonon	i	j	k	l				
ω_{exp}	60	67	100	176				
ω_{cal}	56	65	103	170				

[a]The experimental determination of linewidth for modes e and g has large uncertainties because of their weak signal.

The successful observation of all twelve Raman-active phonons in Fig. 2(m) brings crucial clues for the identification of their eigenvectors. Contrary to an assumption made in previous reports [41,42], the frequencies of the A_g modes are not well separated into a low- and a high-frequency group. Therefore the A_g modes cannot be simply attributed to inter- and intra-ZrTe3-prism vibrations. We hence determined the phonon eigenvectors by first-principles calculations, the result of which is displayed in Figs. 2(a)–2(l), where vibrational patterns are indicated by arrows with lengths proportional to the atomic displacements. Indeed, we find no clear separation of modes by energy. The calculated mode energies are displayed in Table I along with the measured values at $T = 150$ K. This temperature is chosen such that the phonons are least affected by anharmonic lattice interactions (stronger at higher T) and the formation of CDW correlations (stronger at lower T). Despite a slight systematic underestimation in the calculated values by no more than 16 cm^{-1}, the overall agreement between the experimental and computational results is remarkable, rendering our determination of the phonon eigenvectors highly accurate. A one-to-one correspondence between the calculated eigenvectors and the observed Raman peaks is shown in Fig. 2.

C. Phonon linewidths

An important observation in Fig. 2(m) is that the d and f phonon modes exhibit much larger linewidths than the rest. Moreover, the peak of mode d is asymmetric and can be better described by a Fano than a Lorentzian function. It therefore seems likely that these two phonons are strongly coupled to a continuum of excitations, such as electronic excitations. To test this possibility we have performed variable-temperature Raman measurements (Fig. 3). The data are fitted to Lorentzian (modes f and h) and Fano (mode d) functions, and the fit parameters of mode h are also shown for comparison (Fig. 4).

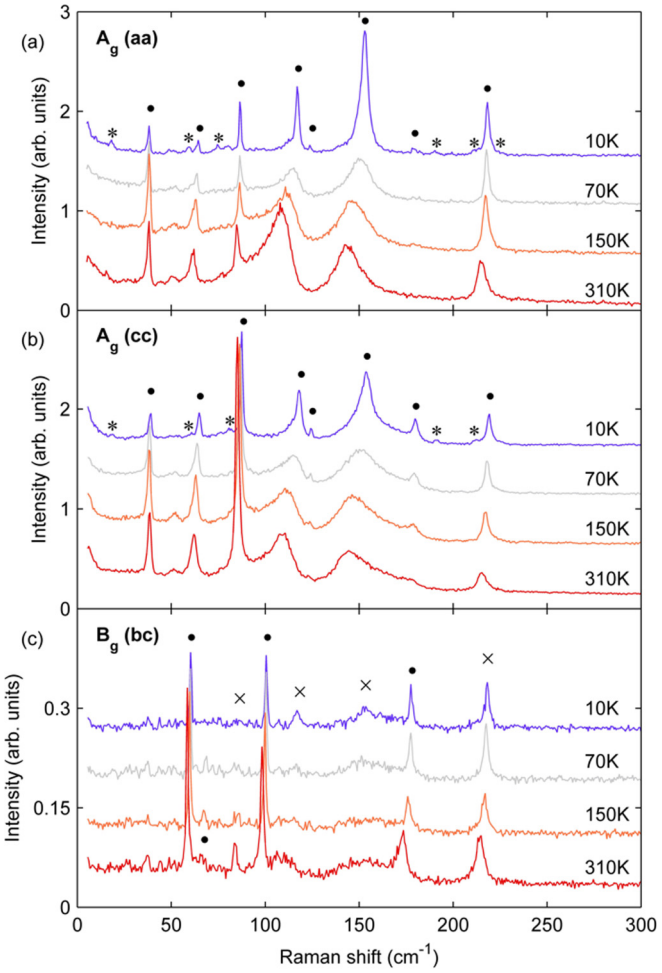

FIG. 3. (Color online) Raman spectra obtained at selected temperatures, offset for clarity. "•" indicates peaks that can be indexed by results shown in Fig. 2, "×" indicates cross-leakage signals due to imperfect polarization of the optical set up and/or defects in the crystal lattice in violation of the structural point-group symmetry, and "∗" indicates additional peaks that appear below T_{cdw}. The additional peaks below T_{cdw}, except for the one at 18 cm^{-1} which is the CDW amplitude mode, are because of Brillouin-zone folding in the CDW phase. The small peak at ∼15 cm^{-1} in the spectrum taken at 310 K in panel (a) should be considered noise and unrelated to the amplitude mode signal, as it is not observed at any intermediate temperatures between T_{cdw} and 300 K.

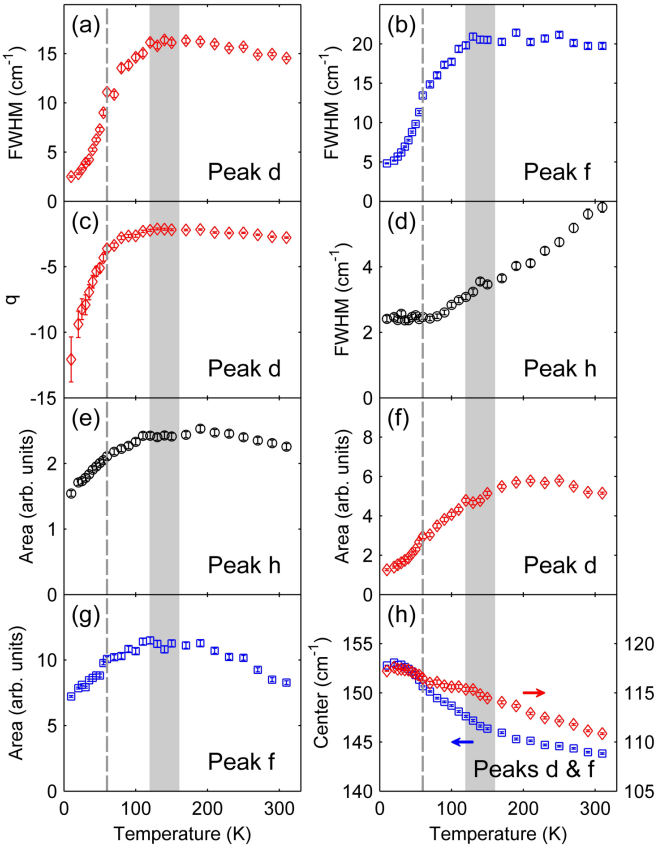

FIG. 4. (Color online) T dependence of fit parameters of selected phonons measured with aa polarizations. Mode indices (d, f, and h) are after those in Fig. 2. Dashed line indicates T_{cdw}. Shaded area indicates T^* with a large uncertainty. The peak areas are displayed after being divided by the Bose factor.

As T decreases, the linewidths (FWHM) of modes d and f are found to decrease substantially [Figs. 4(a) and 4(b)]: the decrease starts already from above T_{cdw} below a characteristic temperature $T^* \approx 140$ K, and is particularly strong near $T = T_{cdw}$. Meanwhile, the asymmetry parameter q in the Fano profile of mode d increases sharply in magnitude as T is decreased below T_{cdw} [Fig. 4(c)], which indicates that the mode rapidly recovers towards a Lorentzian line shape as the CDW order develops. Importantly, both modes d and f involve a longitudinal deformation of the Te(2)-Te(3) chains in their eigenvectors [Figs. 2(d) and 2(f)], which will be discussed in more detail later. For mode h, despite the intermediate linewidth, the fitted FWHM evolves smoothly through T^* and T_{cdw} [Fig. 4(d)]. Also the peak positions of modes d and f do not show clear anomalies near these temperatures [Fig. 4(h)].

We attribute the higher characteristic temperature T^* to the onset of CDW correlations in $ZrTe_3$. A higher onset temperature of short-range correlations than the actual phase transition temperature can be generally expected in low-dimensional systems due to fluctuations. The decrease of phonon linewidths below T^* thus suggests that the electronic states that are coupled to the phonons start to be removed from the Fermi surface by the incipient short-range CDW correlations. This is in qualitative agreement with ARPES results [10], in which T^* is estimated to be above 200 K. In addition to the phonon linewidths, the phonon intensities show a clear departure from the high-T behavior below T^* [Figs. 4(e)–4(g)], which suggests that the local crystal structure starts to deform along with the development of CDW correlations.

The anomalous broadening and Fano asymmetry of the Raman peaks of modes d, f, and h point to strong phonon-electron coupling for these modes, which we are able to confirm with first-principles calculations. The Raman linewidth is estimated as a weighted average of the imaginary part of the phonon self-energy of all small-q phonons involved in the scattering of Raman photons in different directions (see Sec. III C). The calculated phonon linewidths are listed in

Table I along with experimental values, and a semiquantitative agreement is found. In particular, we are able to obtain the three broadest peaks correctly in the computation, a result that does not depend on the detailed choice of the **q** region or the weighing function. This agreement again confirms that the our method of calculation accurately describes the electronic structure and lattice dynamics of $ZrTe_3$, which allows us to ask and answer the questions: Which Bloch states are coupled strongly with the lattice dynamics, and how are they related to the CDW order in this material? Another surprising observation is that mode f shows a pronounced anisotropy in its linewidth when the sample is illuminated from different directions, which is semiquantitatively reproduced by the calculations. We shall return to these shortly.

D. Electronic Raman signal

To further examine the relationship between the opening of electronic energy gaps due to CDW correlations and the change in phonon-electron coupling, we first note that, especially in the aa-polarized Raman spectra in Fig. 3(a), the background intensity exhibits an anomalous decrease with decreasing T. This has also been pointed out in a recent report [42]. The highly accurate data in Fig. 3 allow us to fit all the phonon peaks and systematically remove them from the Raman spectra, a procedure that most clearly reveals the underlying electronic signals. Upon doing so, we find that there are further structures in the data, as shown in Fig. 5(a). Below $\sim$100 cm^{-1}, the change of the electronic signal mainly occurs below T_{cdw}, whereas the change between $\sim$100 and 300 cm^{-1} occurs over a much wider T range, up to T^*. This can be seen from integration of the electronic signal over different energy ranges [Fig. 5(b)].

In an attempt to correlate the electronic signal with the change of phonon-electron coupling versus T, we notice that the electronic signal [Fig. 5(b)] exhibits a similar T dependence to that of the linewidths of phonons d and f [Figs. 4(a) and 4(b)]. Upon changing the energy-integration window, the degree of similarity varies, and the best agreement is found when we integrate the electronic signal up to 150 cm^{-1} [Fig. 5(c)]. This "optimal" upper energy limit is in fact commensurate with the phonon energy scale. It implies that the phonons are damped by electronic excitations that are of lower energies than the phonon energies themselves. In addition to the linewidths, we find that the inverse of the Fano asymmetry parameter q for phonon d, which describes the peak's departure from a Lorentzian line shape due to coupling to an excitation continuum [43], is roughly proportional to the electronic signal's amplitude over nearly a decade of change [Fig. 5(d)]. The extrapolation of $1/q$ to zero in the limit of no electronic excitations suggests that the phonon would fully recover its Lorentzian line shape in the complete absence of phonon-electron coupling.

E. Momentum-resolved phonon-electron coupling matrix elements

In order to reach a concrete and microscopic understanding of the results presented above, we have computed the phonon-electron coupling matrix elements for phonons near the BZ

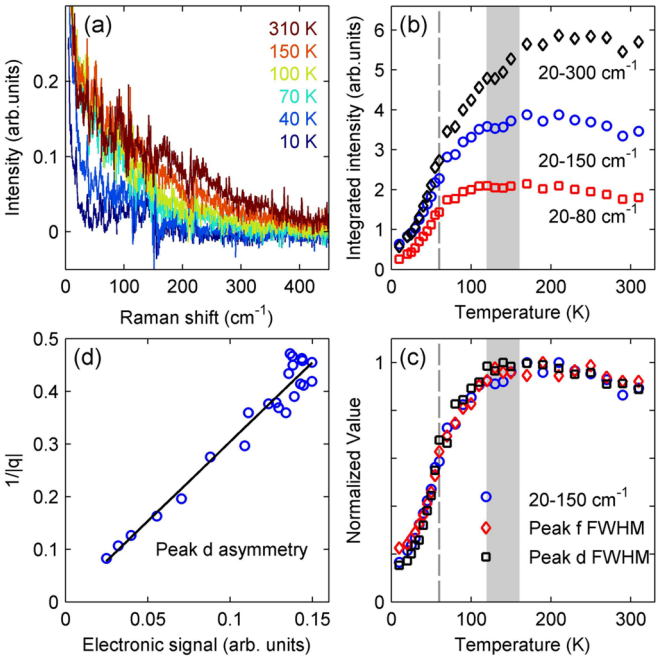

FIG. 5. (Color online) (a) aa-polarized Raman data at selected temperatures after subtracting phonon peaks. (b) Integrated intensities in (a) over different energy ranges. Dashed line and shaded area indicate T_{cdw} and T^*, respectively, the same as in Fig. 4. (c) T dependence of the electronic signal integrated between 20 and 150 cm^{-1}, plotted together with that of the FWHMs of phonon peaks d and f [Figs. 4(a)–4(b)]. Data are normalized at high temperatures. (d) Inverse of Fano asymmetry parameter for phonon d versus the electronic signal integrated between 20 and 150 cm^{-1}, with T being an implicit parameter. Solid line is a linear fit.

center, as functions of the electronic band index and momentum **k** [34]. Figure 6(b) displays our computed Fermi surfaces, which consist of two main sectors [10,16]: A quasi-1D sector forms nearly parallel slabs running perpendicular to $\mathbf{a}^*$, which would indeed favor nesting with $\mathbf{q}_n \approx \mathbf{q}_{cdw} = (0.07,0,0.33)$. The other sector is located primarily in the vicinity of the a^*-c^* plane. Four electronic bands contribute to the Fermi surfaces. They are marked with indices 1, 2, 3, and 4 in Fig. 6(f), where their energy ranges are shown relative to the Fermi level. The quasi-1D sector of the Fermi surface located near the BZ boundary is derived from bands 3 and 4, which mainly arise from the $5p$ orbitals of the Te(2)/Te(3) atoms [Fig. 1(a)].

Indeed, we find that the computed phonon linewidths are dominated by intraband transitions, especially within bands 3 and 4. An electronic wave vector **k** that makes large contributions to the linewidth should satisfy two conditions: (1) the matrix element $|g^{\nu}_{\boldsymbol{kn},\boldsymbol{kn}}|^2$ is large, and (2) the electronic energy $\epsilon_{\boldsymbol{kn}}$ is sufficiently close to the Fermi level. To delineate the contributions to phonon linewidths from individual bands and different sectors of the Fermi surface, isosurfaces of intraband-transition contributions to the matrix elements for phonons d, f, and h are visualized in Figs. 6(c)–6(e), respectively. Figures 6(g)–6(i) display the corresponding value ranges of $|g^{\nu}_{\boldsymbol{kn},\boldsymbol{kn}}|^2$ arising from bands $n = 1$–4, relative to the isovalue for making the isosurfaces. It can be seen, strikingly, that the phonons d and f are most significantly coupled to

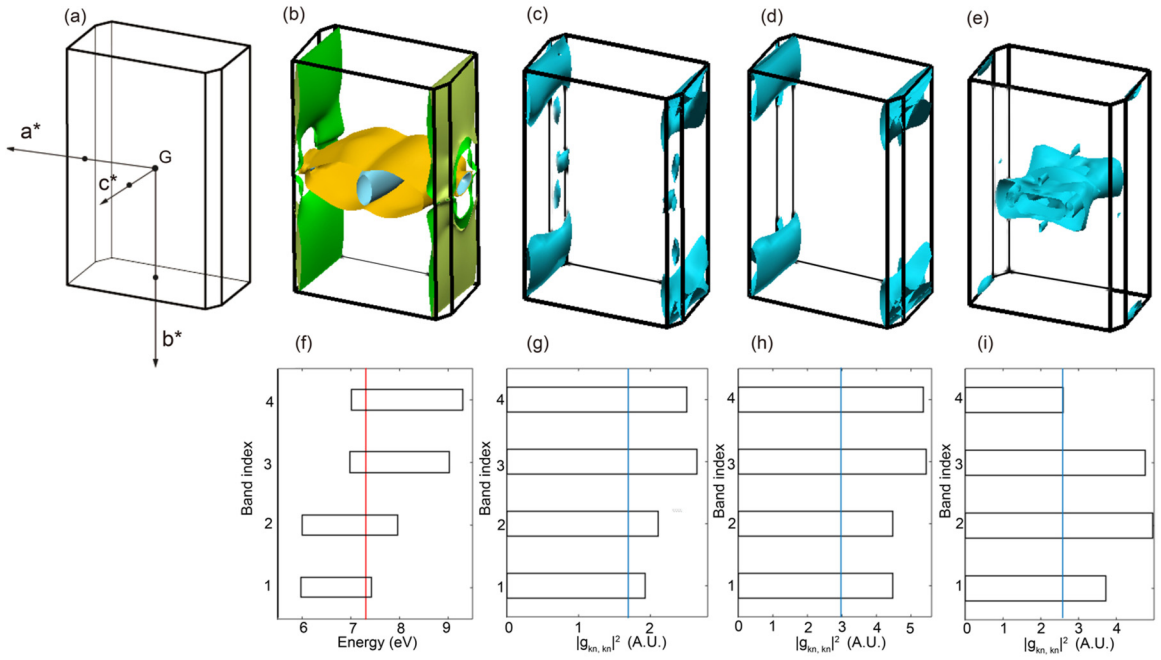

FIG. 6. (Color online) (a) BZ of $ZrTe_3$. (b) Calculated Fermi surfaces. (f) is the corresponding energy locations of the bands across Fermi level (vertical line), marked by indices 1, 2, 3, and 4. (c)–(e) Isosurfaces of $|g^{\nu}_{\boldsymbol{kn},\boldsymbol{kn}}|^2$ for phonon modes d, f, and h in the BZ, with contributions from different bands relative to the chosen isovalues (vertical line) displayed in (g)–(i), respectively. The values of $|g^{\nu}_{\boldsymbol{kn},\boldsymbol{kn}}|^2$ are magnified to similar amplitudes for easier visualization. The angle of view in (b)–(e) is similar to that in (a).

the electronic states near the boundary of the quasi-1D Fermi surfaces. It is not a coincidence that the CDW electronic gap is opened precisely in this region of the BZ [10], and we believe that it is this region of the BZ that makes the greatest contribution to the overall phonon-electron coupling, including to that of the acoustic phonon whose softening to zero frequency triggers the CDW transition (see below). The correspondence between the **k** regions shown in Figs. 6(c) and 6(d) and the gap-opening regions reported in Ref. [10] suggests that the phonon-electron coupling matrix elements dictate the opening of electronic gaps on the Fermi surface.

A remarkable commonality between phonons d and f is the involvement of longitudinal deformations of the Te(2)-Te(3) chains in their eigenvectors [Figs. 2(d) and 2(f)]. In contrast, phonons that do not involve similar atomic displacements (Fig. 2) all have narrow linewidths. This can be intuitively understood, since it is the Te(2)-Te(3) chain that makes a major contribution to the electronic states near the Fermi level. The only exception is mode h, which also involves a deformation of the Te(2)-Te(3) chain but does not exhibit a very large linewidth. This is explained by the fact that the main contributions to $|g^{\nu}_{\boldsymbol{kn},\boldsymbol{kn}}|^2$ are from other regions of the BZ [Fig. 6(e)], and a considerable portion of those are not on the Fermi surface [Fig. 6(b)]. It is hence no surprise that the linewidth of mode h does not show any pronounced anomaly near $T_{\rm cdw}$ or T^* [Fig. 4(d)]; in contrast, a dramatic decrease of the linewidths and a recovery of a Lorentzian line shape are found for mode d and f after the electronic gap opens below T^* (Fig. 3).

A detailed comparison of the aa- and cc-polarization Raman spectra in Fig. 2(m) and Fig. 3 reveals that the measured linewidth of phonon f is different between the two configurations, which correspond to the use of incident photons propagating along the $\mathbf{c}^*$ and $\mathbf{a}^*$ directions, respectively. This difference is rather unexpected, and we are not aware of any previous report of similar effects. It suggests that the phonon linewidth sensitively depends on $\mathbf{q}$ very close to the BZ center, which we are able to reproduce in our computation (Table I) by choosing different $\mathbf{q}$ regions for the weight-average estimate of the linewidth. The key to the "anisotropy" of Raman linewidth is the small but nonzero momentum of incident light in the lattice frame. Different direction of light incidence leads to a different sphere of action in the momentum space, on the surface of which phonons contribute to the observed Raman signal (see Sec. II C for a detailed description of our model). Therefore, when Raman signals are collected with symmetry-inequivalent directions of light incidence, one would generally expect "anisotropy" in the observed phonon linewidth.

The extent of such anisotropy depends on the actual anisotropy in the phonon-electron coupling (provided this is a dominant factor of the phonon lifetimes). Specifically, the phonon-electron coupling for the f phonon branch mainly arises from the boundary of the quasi-1D Fermi surface as depicted in Fig. 6(d), because this part of the Fermi surface is most sensitive to lattice distortions that correspond to the eigenvector of the phonon [Fig. 2(f)]. In this case, the phonon linewidth should be strongly anisotropic because of the pronounced electronic anisotropy near the Fermi surface. The corresponding Fermi velocity lies primarily along $\mathbf{a}^*$. Consequently, phonons on the f branch with momenta that have a larger component along $\mathbf{a}^*$ will experience stronger scattering with conduction electrons, causing intraband transitions in the latter by satisfying $\mathbf{q}\cdot\mathbf{v}_{\rm F}\approx\omega_{\mathbf{q}\nu}$, where $\omega_{\mathbf{q}\nu}$ is the phonon

frequency. Considering the model we propose in Sec. II C, the phonon linewidth of mode f is hence expected to be larger when the light incidence is along the $\mathbf{a}^*$ direction. The fact this experimental observation is reproduced in the DFT-linear response simulation is rather remarkable.

Despite the apparent similarity in the matrix elements of phonons d and f [Figs. 6(c) and 6(d)], it turns out that the sampling for phonon d does not have a strong dependence on the $\mathbf{q}$ regions considered in our computation. While this result nicely corresponds to our experimental observation (Table I), it does depend on computational details including the precise band structure near the Fermi level, the shape and size of the sampling $\mathbf{q}$ region, and the weighing function, all of which are not known *a priori*. Therefore the agreement should be taken only at a semiquantitative level.

According to the above interpretation, the observation of different phonon linewidths with different incident-light directions requires the material system to have specific characteristics. First, the phonon linewidth must be large, and it must arise primarily from phonon-electron coupling that involves electronic intraband transitions, i.e., not from defects or anharmonic lattice interactions. Second, the main contributions to the coupling must come from a highly anisotropic part of the Fermi surface, such that the distribution of pertinent $\mathbf{v}_F$ has a preferential direction. Failure to conform with the second requirement explains why phonon h does not exhibit a similar linewidth anisotropy—the coupling matrix elements are large on the isotropic sectors of the Fermi surface [Figs. 6(b) and 6(e)]. Finally, we note that the above two requirements are in perfect accordance with the characteristics of a "good" CDW system, so it is not a coincidence that we can first observe the effect in $ZrTe_3$, which has arguably the simplest crystal structure (and hence phonon spectrum) among all quasi-1D CDW materials known to date.

F. The CDW amplitude excitation

So far we have only discussed $q = 0$ phonons which cannot be directly responsible for the CDW transition. In a recent x-ray scattering measurement of $ZrTe_3$, a pronounced Kohn anomaly was found on the mostly transverse acoustic phonon branch with polarization along the $\mathbf{a}^*$ direction [44]. The freezing of this mode to zero frequency was suggested to be the triggering factor for the CDW formation. To further confirm this interpretation, we have searched for so-called CDW amplitude excitation, which can be generally expected in materials that undergo incommensurate structural transitions including CDW and other forms of charge ordering [20,45–47]. Such transitions can be generically understood as triggered by an anomalous phonon that freezes to zero frequency. Deeply in the structurally distorted phase, because the structural instability becomes fully relaxed and/or the electronic states that exert damping on the anomalous phonon become mostly gapped out, the frequency of the amplitude excitation is usually found to be close to that of the original (unrenormalized) phonon. In this regard, measurement of the amplitude-excitation frequency can be used to identify the key phonon. To our knowledge, CDW amplitude excitation has not been reported for $ZrTe_3$.

Indeed, a close inspection of the low-energy part of the Raman spectra in Fig. 3(a) suggests the development of a new

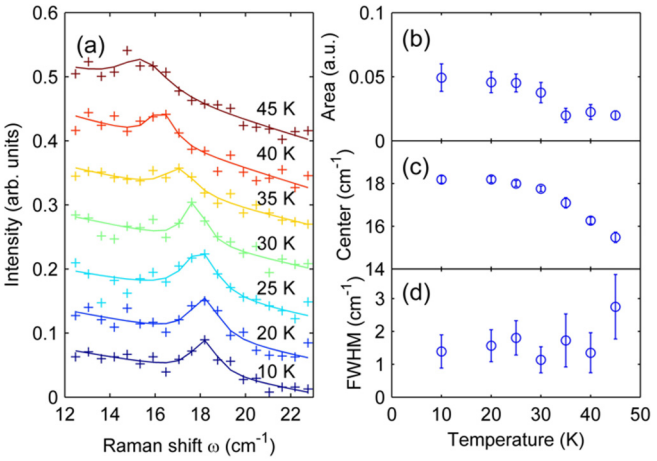

FIG. 7. (Color online) (a) Raman spectra obtained with *aa* polarizations at low temperatures, offset for clarity. (b)–(d) T dependence of fit parameters in (a). The peak areas in (b) are displayed after dividing by the Bose factor.

peak below 20 cm^{-1} at $T = 10$ K. We have measured this feature with very high counting statistics at low T [Fig. 7(a)], and above $T = 45$ K we can no longer resolve it above the diffused-scattering background. By fitting the peak to a Lorentzian profile, we have obtained its key parameters as functions of T [Figs. 7(b)–7(d)]. In particular, its energy softens by over 10% upon heating from 10 K to 45 K. While such an amount of softening is considerably smaller than those observed in quasi-2D [17] and 3D materials [47], it is not uncommon among quasi-1D systems [48]. Therefore we attribute this feature to the CDW amplitude excitation. Importantly, its frequency (18 cm^{-1}) at 10 K amounts to about 2.2 meV, not far from the unrenormalized energy (≈2.5 meV) of the Kohn anomaly at high temperatures [44]. This further confirms that, indeed, it is the acoustic phonon that involves the deformation of the Te(2)-Te(3) chains along the a axis that triggers the CDW transition at T_{cdw}.

IV. CONCLUDING REMARKS

In summary, we have performed polarized Raman measurements on $ZrTe_3$, the results of which are compared back-to-back with our first-principles calculations. The latter has allowed us to unequivocally determine the phonon eigenvectors as well as the phonon-electron coupling matrix elements, which have remained hitherto unknown for this model quasi-1D CDW compound. Our result demonstrates that particular lattice vibrational patterns, namely, the longitudinal deformations of the Te(2)-Te(3) chains, exhibit strong interactions with the conduction electrons. Such interactions appear to play an essential role, in conjunction with the strong FSN, in the formation of CDW order in this quasi-1D system.

As a joint consequence of the highly anisotropic electronic structure and strong phonon-electron coupling in $ZrTe_3$, we have identified a distinct Raman scattering phenomenon, where the measured phonon linewidths can pronouncedly depend on the direction of the incident light, contrary to the usual understanding that Raman scattering is a $q = 0$ probe. Similar effects can be expected to exist in other

low-dimensional CDW materials, where the pertinent requirements are most likely to be conformed with simultaneously.

We emphasize that our calculations are for $q \approx 0$ phonons only. Our results about the phonon-mode and electron-**k** dependence of the phonon-electron coupling matrix elements do not rely on the FSN geometry, but such dependencies should be important to consider for phonons with $\mathbf{q} \approx \mathbf{q}_{\mathrm{cdw}}$ as well, as they will cast a strong influence on the formation of CDW order. In particular, we believe that it is the matrix elements that select out the specific phonon that first freezes to zero frequency, and hence determine the lattice distortions that are associated with the CDW order. Moreover, it is highly likely that the opening of (partial) electronic gaps on the Fermi surface in the CDW phase is dictated by the **k** dependence of the matrix element for the selected phonons, especially when the quality of nesting does not vary substantially across a larger portion of the Fermi surface. We emphasize that phonon-electron coupling does play an important role in the CDW formation. Meanwhile, the contributions of FSN is still to be assessed, and calculations for phonons with $\mathbf{q} \approx \mathbf{q}_{\mathrm{cdw}}$ warrant further investigations and appear necessary for a quantitative understanding of the full microscopic origin of quasi-1D CDW order in a material as simple as $ZrTe_3$.

ACKNOWLEDGMENTS

We wish to thank N. L. Wang and F. Wang for stimulating discussions, and L. C. Wang, C. L. Zhang, and D. W. Wang for their assistance in the synthesis and characterization of $ZrTe_3$ samples. The computational work was performed on TianHe-1(A) at the National Supercomputer Center in Tianjin. This work is supported by the NSF of China (No. 11374024 and No. 11174009) and the NBRP of China (No. 2013CB921903, No. 2011CBA00109, and No. 2013CB921900).

Y.H. and F.Z. contributed equally to this work. Y.L. conceived the research. Y.H., X.R., and Y.L. performed the Raman measurements and other experimental characterizations. F.Z. and J.F. performed the first-principles calculations. Y.L. and J.F. coordinated the project and advised. Y.H, F.Z., J.F., and Y.L. wrote the manuscript with input from all co-authors.

[1] T. Wu, H. Mayaffre, S. Krämer, M. Horvatić, C. Berthier, W. N. Hardy, R. Liang, D. A. Bonn, and M.-H. Julien, Nature (London) **477**, 191 (2011).

[2] G. Ghiringhelli, M. Le Tacon, M. Minola, S. Blanco-Canosa, C. Mazzoli, N. B. Brookes, G. M. De Luca, A. Frano, D. G. Hawthorn, F. He, T. Loew, M. M. Sala, D. C. Peets, M. Salluzzo, E. Schierle, R. Sutarto, G. A. Sawatzky, E. Weschke, B. Keimer, and L. Braicovich, Science **337**, 821 (2012).

[3] R. Comin, A. Frano, M. M. Yee, Y. Yoshida, H. Eisaki, E. Schierle, E. Weschke, R. Sutarto, F. He, A. Soumyanarayanan, Y. He, M. Le Tacon, I. S. Elfimov, J. E. Hoffman, G. A. Sawatzky, B. Keimer, and A. Damascelli, Science **343**, 390 (2014).

[4] W. Tabis, Y. Li, M. Le Tacon, L. Braicovich, A. Kreyssig, M. Minola, G. Dellea, E. Weschke, M. Veit, M. Ramazanoglu, A. Goldman, T. Schmitt, G. Ghiringhelli, N. Barišić, M. Chan, C. Dorow, G. Yu, X. Zhao, B. Keimer, and M. Greven, Nat. Commun. **5**, 5875 (2014).

[5] E. H. da Silva Neto, P. Aynajian, A. Frano, R. Comin, E. Schierle, E. Weschke, A. Gyenis, J. Wen, J. Schneeloch, Z. Xu, S. Ono, G. Gu, M. Le Tacon, and A. Yazdani, Science **343**, 393 (2014).

[6] J. M. Tranquada, B. J. Sternlieb, J. D. Axe, Y. Nakamura, and S. Uchida, Nature (London) **375**, 561 (1995).

[7] T. Timusk and B. Statt, Rep. Prog. Phys. **62**, 61 (1999).

[8] S. V. Borisenko, A. A. Kordyuk, V. B. Zabolotnyy, D. S. Inosov, D. Evtushinsky, B. Büchner, A. N. Yaresko, A. Varykhalov, R. Follath, W. Eberhardt, L. Patthey, and H. Berger, Phys. Rev. Lett. **102**, 166402 (2009).

[9] V. Brouet, W. L. Yang, X. J. Zhou, Z. Hussain, N. Ru, K. Y. Shin, I. R. Fisher, and Z. X. Shen, Phys. Rev. Lett. **93**, 126405 (2004).

[10] T. Yokoya, T. Kiss, A. Chainani, S. Shin, and K. Yamaya, Phys. Rev. B **71**, 140504 (2005).

[11] T. P. Croft, C. Lester, M. S. Senn, A. Bombardi, and S. M. Hayden, Phys. Rev. B **89**, 224513 (2014).

[12] D. LeBoeuf, N. Doiron-Leyraud, B. Vignolle, M. Sutherland, B. J. Ramshaw, J. Levallois, R. Daou, F. Laliberté, O. Cyr-Choinière, J. Chang, Y. J. Jo, L. Balicas, R. Liang, D. A. Bonn, W. N. Hardy, C. Proust, and L. Taillefer, Phys. Rev. B **83**, 054506 (2011).

[13] R. Comès, M. Lambert, H. Launois, and H. R. Zeller, Phys. Rev. B **8**, 571 (1973).

[14] J. P. Pouget, B. Hennion, C. Escribe-Filippini, and M. Sato, Phys. Rev. B **43**, 8421 (1991).

[15] D. DiCarlo, R. E. Thorne, E. Sweetland, M. Sutton, and J. D. Brock, Phys. Rev. B **50**, 8288 (1994).

[16] C. Felser, E. Finckh, H. Kleinke, F. Rocker, and W. Tremel, J. Mater. Chem. **8**, 1787 (1998).

[17] J. Tsang, J. Smith Jr., and M. Shafer, Phys. Rev. Lett. **37**, 1407 (1976).

[18] B. F. Hu, B. Cheng, R. H. Yuan, T. Dong, and N. L. Wang, Phys. Rev. B **90**, 085105 (2014).

[19] R. Peierls, *Quantum Theory of Solids* (Oxford University, New York, 1955).

[20] G. Grüner, *Density Waves in Solids* (Addison-Wesley, Reading, MA, 1994).

[21] H. Ando, T. Yokoya, K. Ishizaka, S. Tsuda, T. Kiss, S. Shin, T. Eguchi, M. Nohara, and H. Takagi, J. Phys. Condens. Matter **17**, 4935 (2005).

[22] J. Laverock, S. B. Dugdale, Z. Major, M. A. Alam, N. Ru, I. R. Fisher, G. Santi, and E. Bruno, Phys. Rev. B **71**, 085114 (2005).

[23] D. W. Shen, B. P. Xie, J. F. Zhao, L. X. Yang, L. Fang, J. Shi, R. H. He, D. H. Lu, H. H. Wen, and D. L. Feng, Phys. Rev. Lett. **99**, 216404 (2007).

[24] M. D. Johannes, I. I. Mazin, and C. A. Howells, Phys. Rev. B **73**, 205102 (2006).

[25] M. D. Johannes and I. I. Mazin, Phys. Rev. B **77**, 165135 (2008).

[26] W. Kohn, Phys. Rev. Lett. **2**, 393 (1959).

[27] C. M. Varma and A. L. Simons, Phys. Rev. Lett. **51**, 138 (1983).

[28] Y. Ge and A. Y. Liu, Phys. Rev. B **82**, 155133 (2010).
[29] L. P. Gor'kov, Phys. Rev. B **85**, 165142 (2012).
[30] H.-M. Eiter, M. Lavagnini, R. Hackl, E. A. Nowadnick, A. F. Kemper, T. P. Devereaux, J.-H. Chu, J. G. Analytis, I. R. Fisher, and L. Degiorgi, Proc. Natl. Acad. Sci. USA **110**, 64 (2013).
[31] F. Weber, S. Rosenkranz, J.-P. Castellan, R. Osborn, R. Hott, R. Heid, K.-P. Bohnen, T. Egami, A. H. Said, and D. Reznik, Phys. Rev. Lett. **107**, 107403 (2011).
[32] C. J. Arguello, E. P. Rosenthal, E. F. Andrade, W. Jin, P. C. Yeh, N. Zaki, S. Jia, R. J. Cava, R. M. Fernandes, A. J. Millis, T. Valla, R. M. Osgood, and A. N. Pasupathy, Phys. Rev. Lett. **114**, 037001 (2015).
[33] R. Seshadri, E. Suard, C. Felser, E. W. Finckh, A. Maignan, and W. Tremel, J. Mater. Chem. **8**, 2869 (1998).
[34] P. Giannozzi, S. Baroni, N. Bonini, M. Calandra, R. Car, C. Cavazzoni, D. Ceresoli, G. L. Chiarotti, M. Cococcioni, I. Dabo, A. Dal Corso, S. de Gironcoli, S. Fabris, G. Fratesi, R. Gebauer, U. Gerstmann, C. Gougoussis, A. Kokalj, M. Lazzeri, L. Martin-Samos, N. Marzari, F. Mauri, R. Mazzarello, S. Paolini, A. Pasquarello, L. Paulatto, C. Sbraccia, S. Scandolo, G. Sclauzero, A. P. Seitsonen, A. Smogunov, P. Umari, and R. M. Wentzcovitch, J. Phys. Condens. Matter **21**, 395502 (2009).
[35] X. Zhu, B. Lv, F. Wei, Y. Xue, B. Lorenz, L. Deng, Y. Sun, and C.-W. Chu, Phys. Rev. B **87**, 024508 (2013).
[36] L. Hedin and B. Lundqvist, J. Phys. C **4**, 2064 (1971).
[37] J. P. Perdew, K. Burke, and M. Ernzerhof, Phys. Rev. Lett. **77**, 3865 (1996).
[38] C. Hartwigsen, S. Goedecker, and J. Hutter, Phys. Rev. B **58**, 3641 (1998).
[39] S. Herr and J. Brill, Synth. Met. **16**, 283 (1986).
[40] X. Zhu, H. Lei, and C. Petrovic, Phys. Rev. Lett. **106**, 246404 (2011).
[41] A. Zwick, M. Renucci, and A. Kjekshus, J. Phys. C **13**, 5603 (1980).
[42] S. L. Gleason, Y. Gim, T. Byrum, A. Kogar, P. Abbamonte, E. Fradkin, G. J. MacDougall, D. J. Van Harlingen, X. Zhu, C. Petrovic, and S. L. Cooper, arXiv:1501.06871.
[43] U. Fano, Phys. Rev. **124**, 1866 (1961).
[44] M. Hoesch, A. Bosak, D. Chernyshov, H. Berger, and M. Krisch, Phys. Rev. Lett. **102**, 086402 (2009).
[45] J. F. Scott, Rev. Mod. Phys. **46**, 83 (1974).
[46] H. Z. Cummins, Phys. Rep. **185**, 211 (1990).
[47] X. Du, R. Yuan, L. Duan, C. Wang, Y. Hu, and Y. Li, Phys. Rev. B **90**, 104414 (2014).
[48] D. Sagar, D. Fausti, S. Yue, C. Kuntscher, S. van Smaalen, and P. van Loosdrecht, New J. Phys. **10**, 023043 (2008).